OMTM, Volume *31*

Supplemental information

Multiparametric domain insertional profiling of adeno-associated virus VP1

Mareike D. Hoffmann, Alina C. Zdechlik, Yungui He, David Nedrud, George Aslanidi, Wendy Gordon, and Daniel Schmidt

Note S1: Linking clusters to AAV function

Using existing AAV structure / function relationships knowledge, we can begin to make association between each of the five identified clusters and their specific roles in AAV packaging and infection:

1. The strong association between poor pulldown fitness, uptake fitness, and cluster 1 is obvious considering it being comprised of mostly buried or internal residues and containing VP1u, which encodes the required PLA2 domain and nuclear localization signals.[1–4] Conversely, association with higher packaging fitness would be compatible with motif insertion promoting externalization of VP1u, thus decreasing steric hindrance with the packaged genome.

2. The sensitivity of cluster 3 with respect to packaging efficiency is consistent with trimer formation and stability, which are key determinants of capsid assembly.[5, 6] Most binding sites for cellular receptors (e.g., proteoglycan, AAVR) are located near the 3-fold axis, as well.[7–13] Flexibility of the 2-fold interface has previously been linked not only to AAV infectivity[14], but also genome packaging[15], which would explain how insertions may drive poor packaging fitness.

3. The relatively neutral fitness of cluster 2 (e.g., packaging, uptake) is consistent with most insertions ending up on the capsid interior, not interfering with assembly or cellular uptake. While the 5-fold pore is part of this cluster, a numeric simulation of VP1 copy numbers ranging from 1-10 suggests that around half of the twelve 5-fold pores are assembled from non-VP1 only, and thus available as an alternative pathway for Rep-mediated genome packaging.

4. Cluster 5 has an intricate structure, with the HI loops that surround the 5-fold pore like the blades of an aperture and connecting to the base of the 3-fold axis. Prior studies that have suggested a link between conformational changes at the 3-fold protrusion upon binding cell surface proteoglycan are communicated to conformational change at the 5-fold pore, priming the release of VP1u.[16]

Note S2: Effects of cysteine mutants

Several of the cysteine pairs we hand-picked involve interfaces that undergo conformational dynamics during infection:

1. Mutating F671C in the HI loop was strongly deleterious to infection, but this phenotype was rescued in the background of H255C, which by itself was benign. Prior studies have shown that heparin binding near the 3-fold and 2-fold axes induces an HI loop re-arrangement and an iris-like opening of the channel located at the 5-fold axis.[16] HI loop deletions, substitutions, and insertions have shown that this loop, while flexible in amino acid composition and length, is critical for proper VP1 incorporation and infectivity [17]. The same study showed that interaction of the HI loop with the underlying EF loop is mediated by hydrophobic pi-stacking interactions (F661/P373; in AAV2 numbering) and that disrupting this interaction lowers infectivity by preventing VP1 incorporating into assembled capsid. Our results are reminiscent of this mechanism.

2. Positions F671/H255, which can form NH···π hydrogen bonds, are both conserved across AAV serotypes. H225C may be benign as this supports formation of an aromatic-thiol π hydrogen bond, thus allowing VP1 to incorporate or retaining structural rearrangement after receptor binding. Conversely, F671C is disruptive as it removes the aromatic component of π-stacking interactions, prevents VP1 incorporation and/or disrupts these rearrangements. The H255C/F671C double mutant may rescue infectivity by forming a disulfide bond to substitute as a stand in for π interactions.

3. H423C (at the base of the 3-fold axis) and V613C (with the 2-fold interface) individually had little effect, but together strongly impaired infectivity. This trend held true for adjacent pairs (H360C/437C; H428CL737C) that similar linked clusters comprising the 3-fold protrusion and 2-fold axis. Interestingly, several prior studies have linked AAV infectivity and conformational dynamics at the 3-fold and 2-fold axes. In addition to structural rearrangements in the HI loops, heparin binding to AAV2 causes significant rearrangement of 3-fold protrusions and the 2-fold valleys.[16] Selective oxidation of tyrosine residue at the 2-fold dimer interface lowered infectivity.[14] A mutation (R432A in AAV2) remodeled intramolecular and intermolecular hydrogen bond networks propagating from the 3-fold to both 2-fold and 5-fold axes.[18, 19]

We would like to note here that more factors than an oxidizing environment play a role in the formation of disulfide bonds, including the structure of the protein, but also the surrounding amino acids and the pH value. Furthermore, post-translational modifications other than disulfide bonds can also occur in an oxidizing environment, the effects of which cannot be distinguished from those of disulfide bonds in our experimental approach.

A

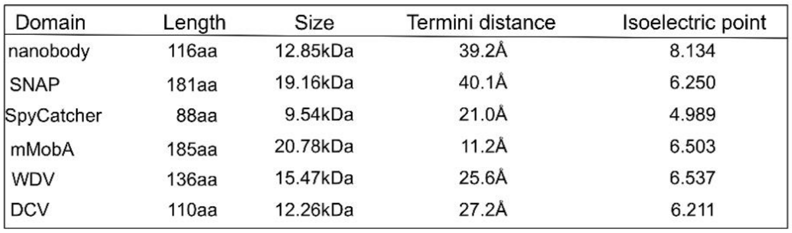

Domain	Length	Size	Termini distance	Isoelectric point
nanobody	116aa	12.85kDa	39.2Å	8.134
SNAP	181aa	19.16kDa	40.1Å	6.250
SpyCatcher	88aa	9.54kDa	21.0Å	4.989
mMobA	185aa	20.78kDa	11.2Å	6.503
WDV	136aa	15.47kDa	25.6Å	6.537
DCV	110aa	12.26kDa	27.2Å	6.211

B

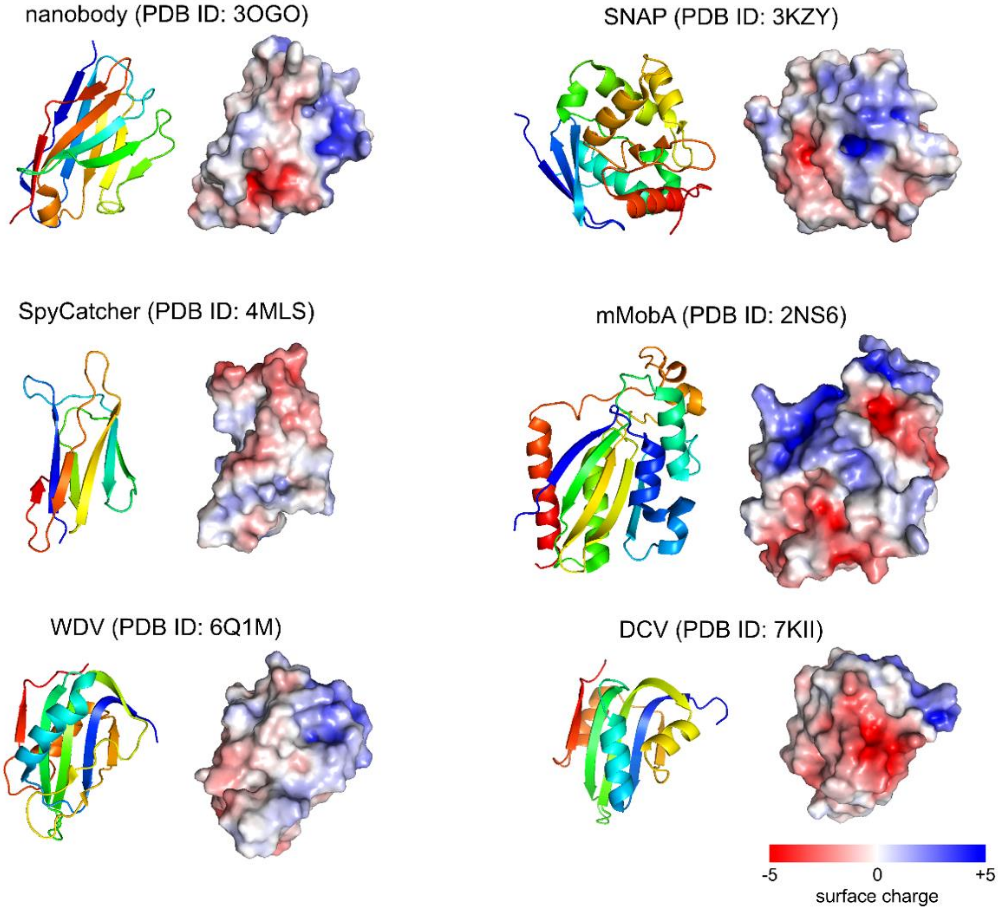

C

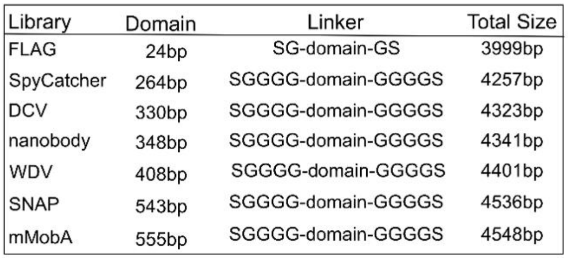

Library	Domain	Linker	Total Size
FLAG	24bp	SG-domain-GS	3999bp
SpyCatcher	264bp	SGGGG-domain-GGGGS	4257bp
DCV	330bp	SGGGG-domain-GGGGS	4323bp
nanobody	348bp	SGGGG-domain-GGGGS	4341bp
WDV	408bp	SGGGG-domain-GGGGS	4401bp
SNAP	543bp	SGGGG-domain-GGGGS	4536bp
mMobA	555bp	SGGGG-domain-GGGGS	4548bp

Figure S1

Properties of inserted domains and sizes of library payloads. (A) Physical descriptions of domains used in this study. (B) Cartoon representation of domain structures (left) and surface representation with net surface charge shown as a gradient from red (negative), over white (neutral), to blue (positive). (C) Sizes of library payloads.

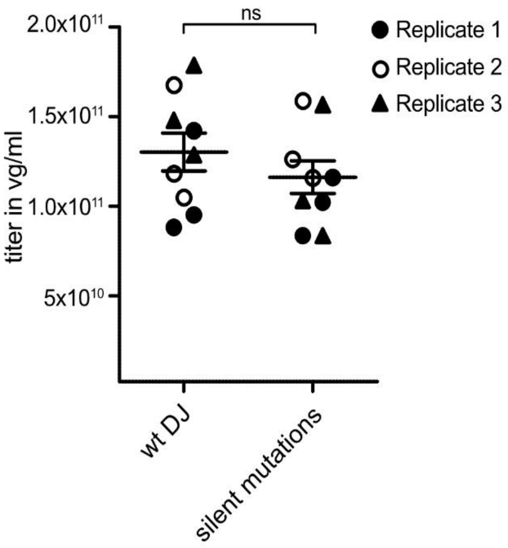

Figure S2

Packaging fitness of silent mutation variant compared to AAV-DJ. Crude lysate packaging titers quantified via qPCR. Three replicates with three technical replicates each were performed. Data are means ± SEM. No statistical significance (ns) between AAV-DJ and the silent mutations variant by an unpaired, two-sided Student's t-test (p-value: 0.3327).

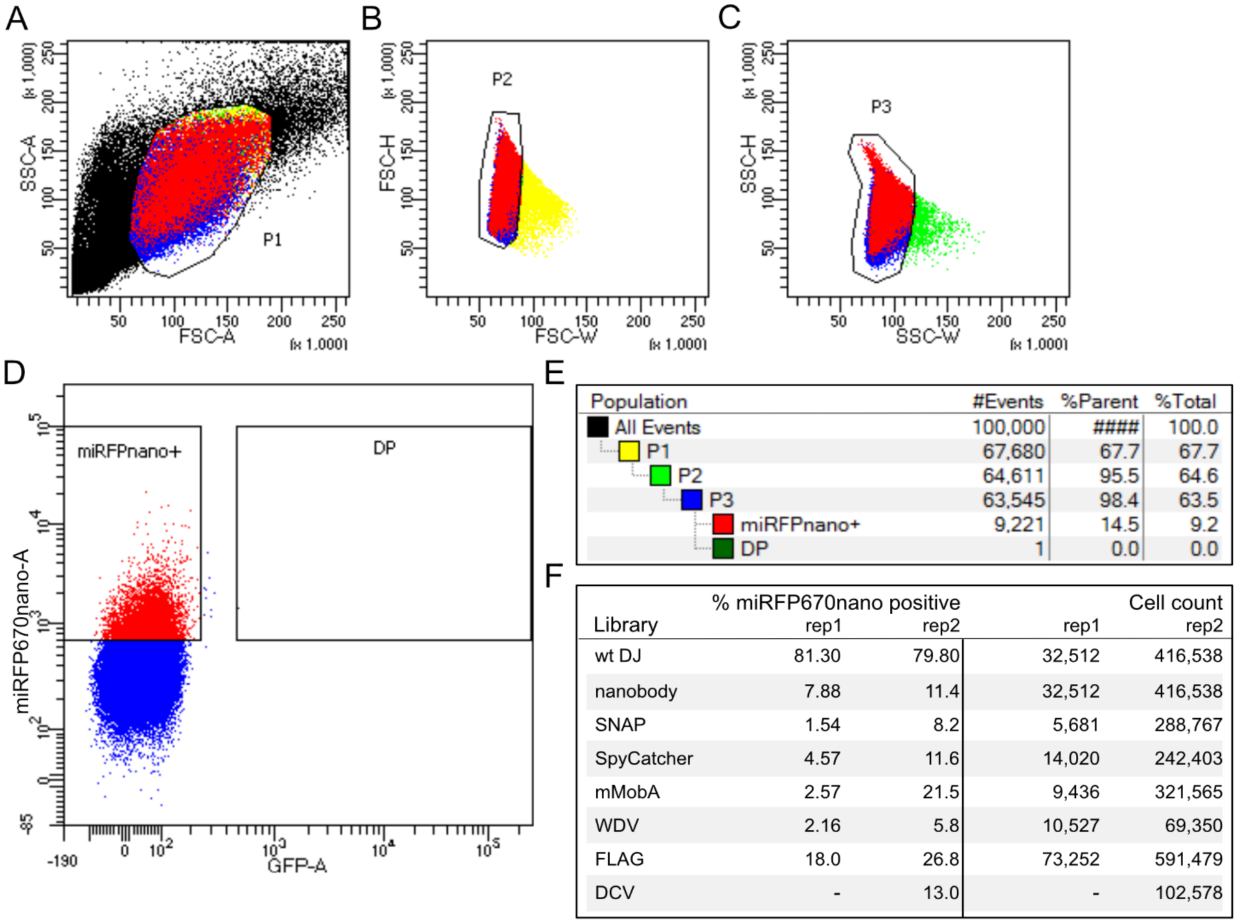

Population	#Events	%Parent	%Total
⬛ All Events	100,000	####	100.0
🟨 P1	67,680	67.7	67.7
🟩 P2	64,611	95.5	64.6
🟦 P3	63,545	98.4	63.5
🟥 miRFPnano+	9,221	14.5	9.2
🟩 DP	1	0.0	0.0

	% miRFP670nano positive		Cell count	
Library	rep1	rep2	rep1	rep2
wt DJ	81.30	79.80	32,512	416,538
nanobody	7.88	11.4	32,512	416,538
SNAP	1.54	8.2	5,681	288,767
SpyCatcher	4.57	11.6	14,020	242,403
mMobA	2.57	21.5	9,436	321,565
WDV	2.16	5.8	10,527	69,350
FLAG	18.0	26.8	73,252	591,479
DCV	-	13.0	-	102,578

Figure S3

Infection fitness assay gating scheme. (A) Whole HEK293FT cells are gated on side (SSC-A) and forward scattering (FSC-A). (B-C) Forward scattering height (FSC-H), forward scattering width (FSC-W), and side scattering width (SSC-W) are used to gate single cells. (D) Cells are further gated using miRFP670nano as an infection marker (representative example). (E-F) Sort statistic for each gated cell population.

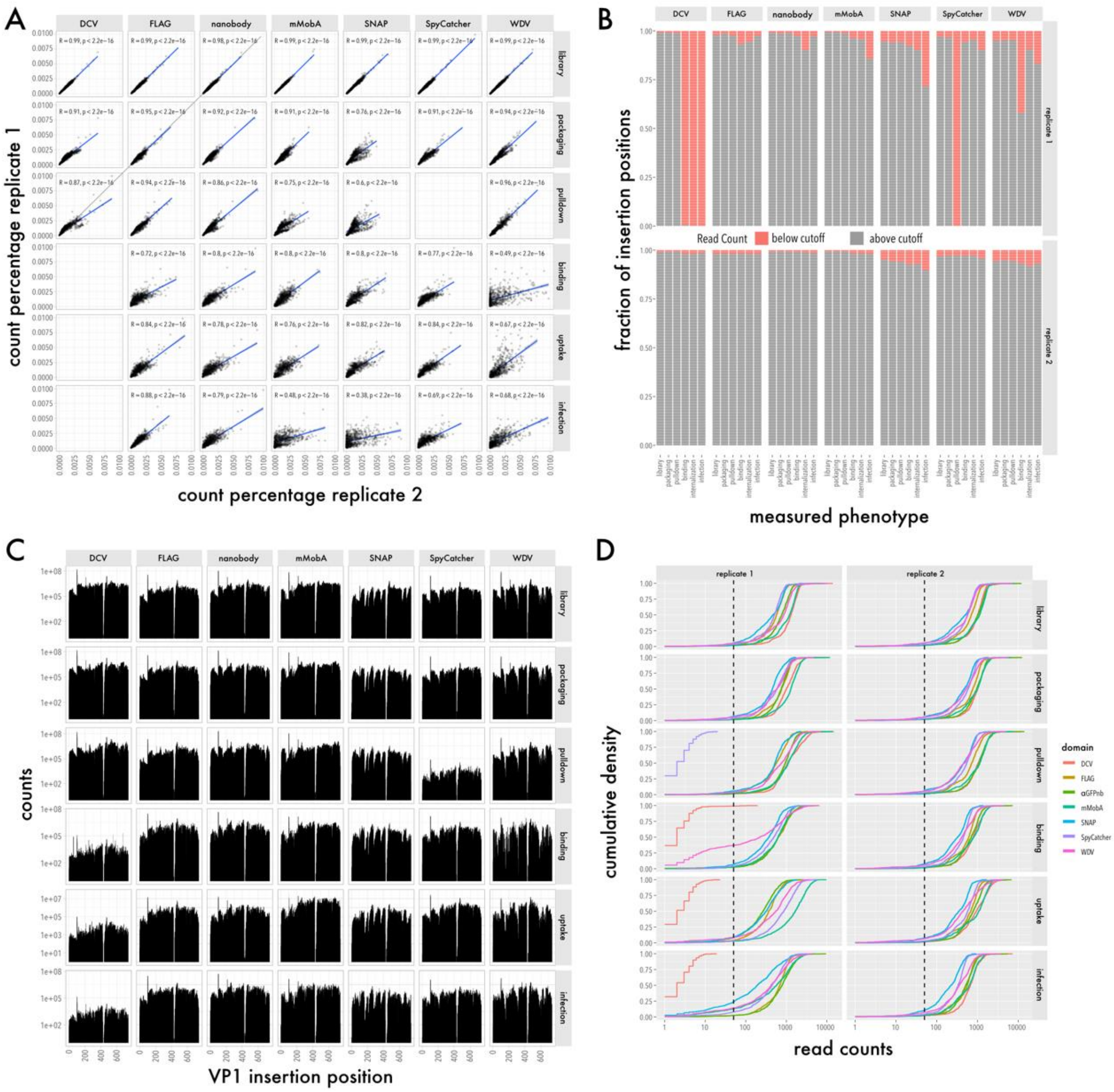

Figure S4

Fitness assay biological replicates, data completeness, and depth. (A) Read counts of replicate 1 are plotted against read counts of replicate 2 for the plasmid library, packaging, pulldown, binding, uptake, and infection assays. Data for all seven inserted domains are shown. Linear correlation was calculated (blue line). Pearson correlation coefficient and p values are shown. (B) Contingency plots showing the fraction of insertion positions below (red) and above (grey) the read count quantity cut-off of 50 reads for all seven domains and measured phenotypes. Data are shown for replicate 1 (top) and replicate 2 (bottom). (C) Total read counts of the plasmid library, packaging, pulldown, binding, uptake, and infection assays for each position are represented by insertion position. Data for all seven inserted domains are shown. (D) Cumulative density plots showing the read counts of the plasmid library, packaging, pulldown, binding, uptake, and infection assays for all seven inserted domains for replicate 1 and replicate 2. Cut off for sufficient read quantity was set to 50 reads and is represented by the black dashed lines.

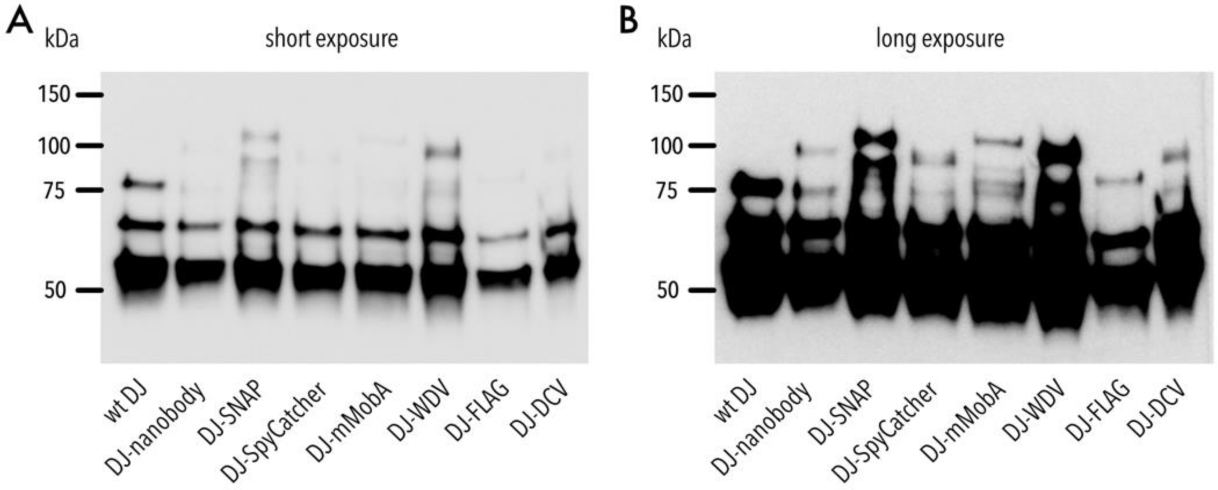

Figure S5

Western blot of AAV domain insertion libraries. (A-B) Representative Western blot image of AAV domain insertion libraries stained with B1 antibody (detecting VP1, VP2 and VP3 subunits) at a short exposure time (A) and long exposure time (B).

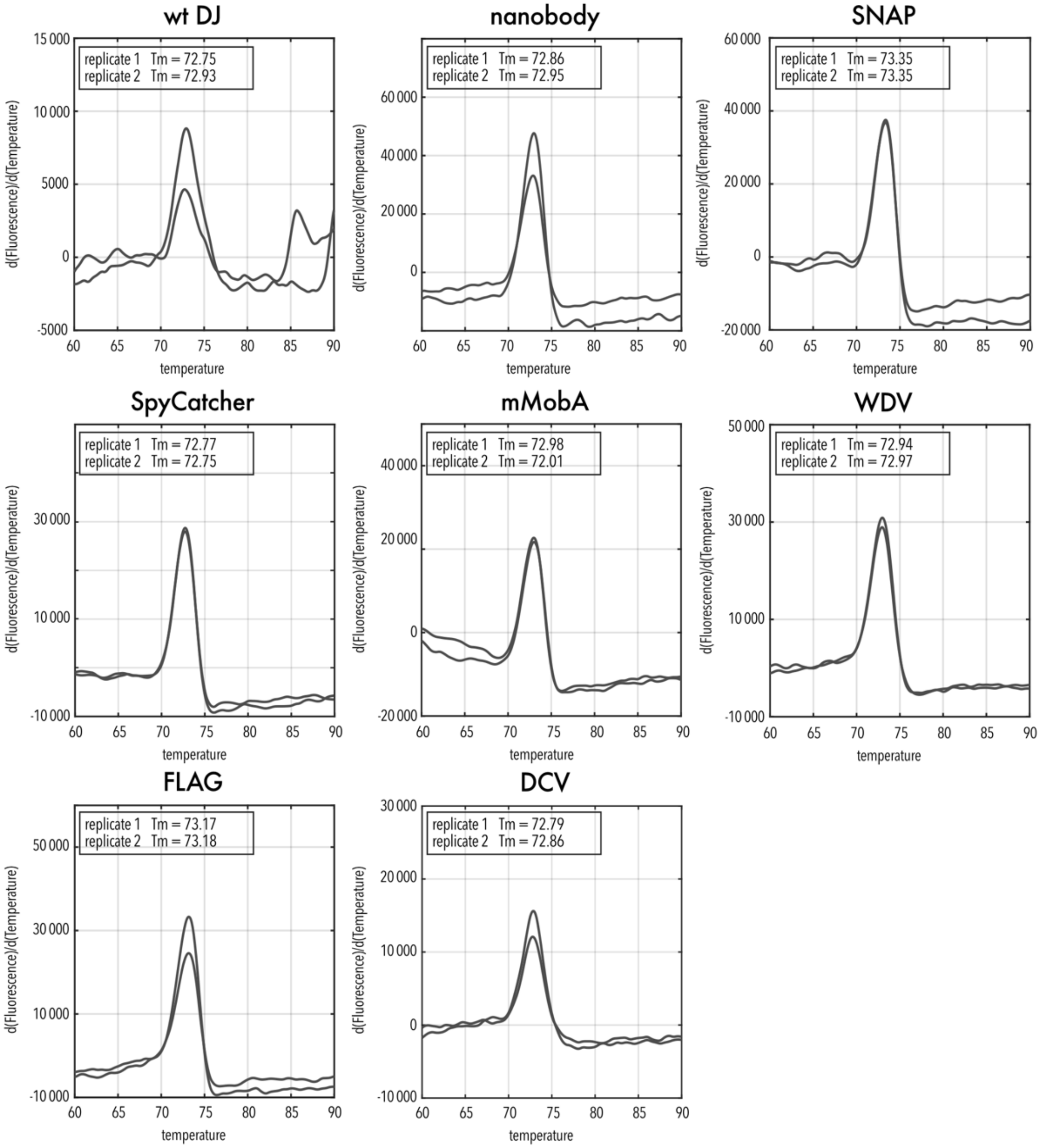

Figure S6

Thermal profiles of AAV domain insertion libraries. Data of two replicates are shown as "∂(Fluorescence)/∂(Temperature)" versus Temperature in °C.

A

sample	full	empty	undecided	total	% full
wt DJ	309	17	18	344	89.8
nanobody	508	48	26	582	87.3
SNAP	377	50	40	467	80.7

B

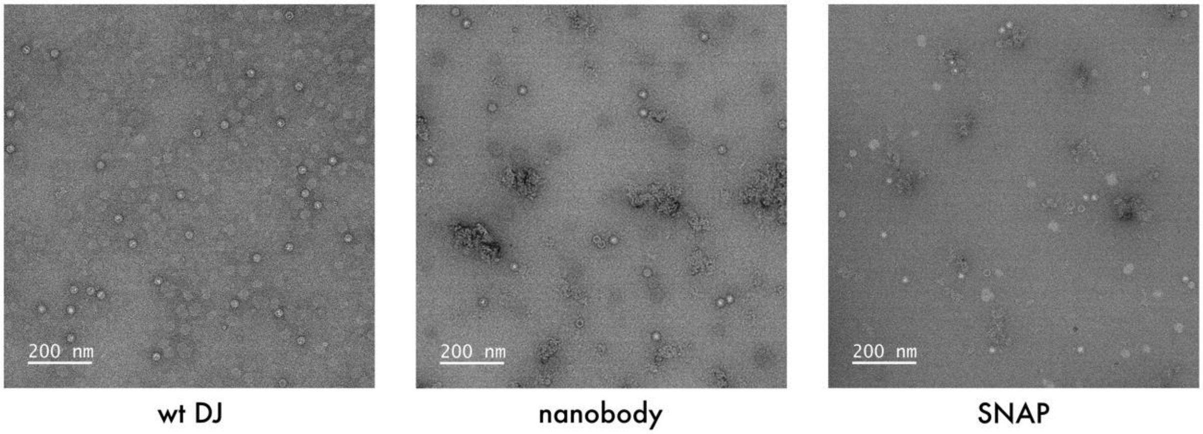

Figure S7

Quantification of empty to full capsid ratio by negative staining transmission electron microscopy. (A) More than 300 capsids were counted manually and grouped into full, empty, and undecided and the percentage of full capsids was calculated. (B) Representative transmission electron microscopy images of the indicated samples.

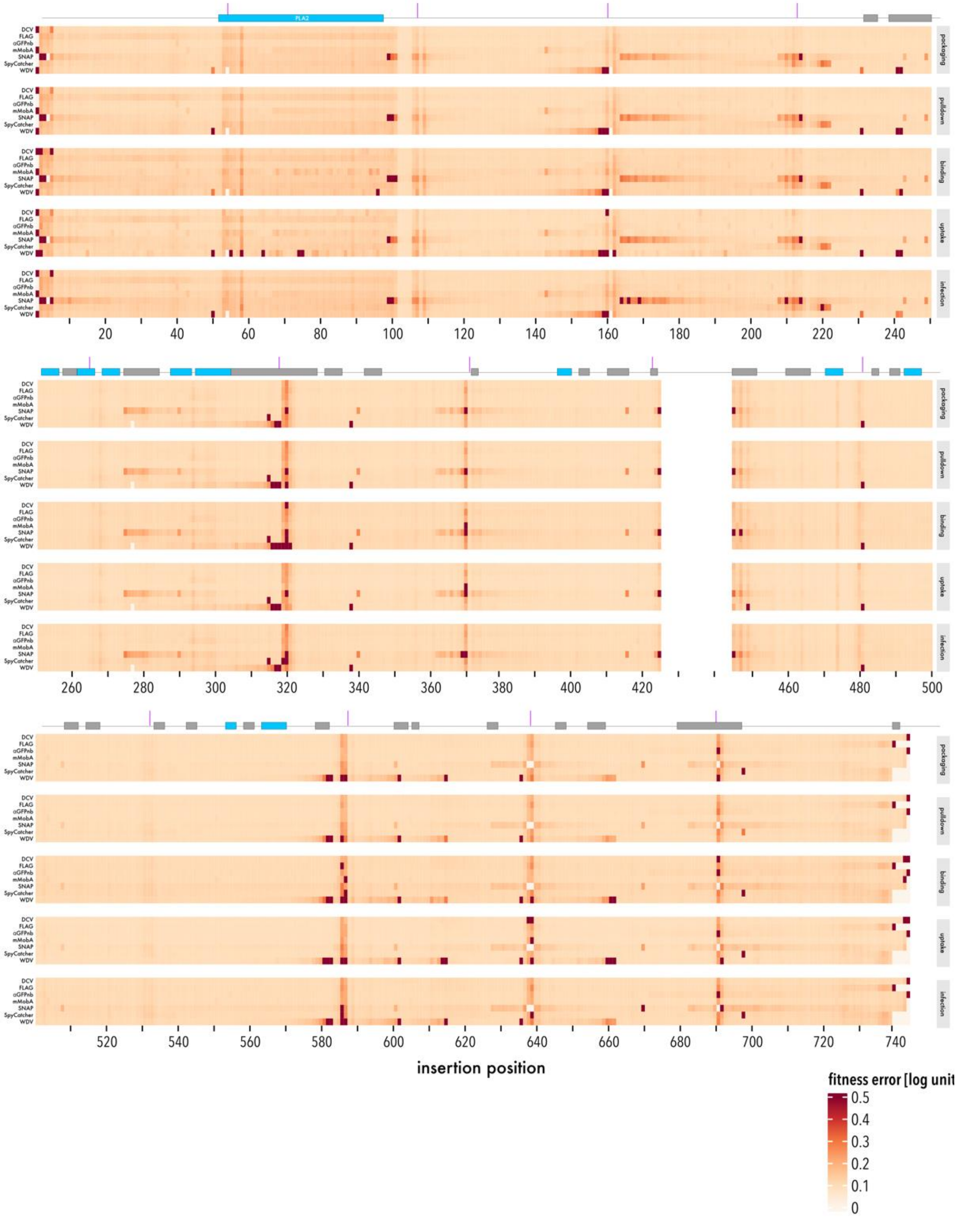

Figure S8

Accuracy of domain insertional profiling data. Standard errors of AAV fitness of all seven domain insertion libraries by insertion position and fitness assay. Secondary structure elements and VR1-9 of the capsid are indicated on top. Boundaries of oligos from VP1 assembly using SPINE are indicated by purple vertical bars.

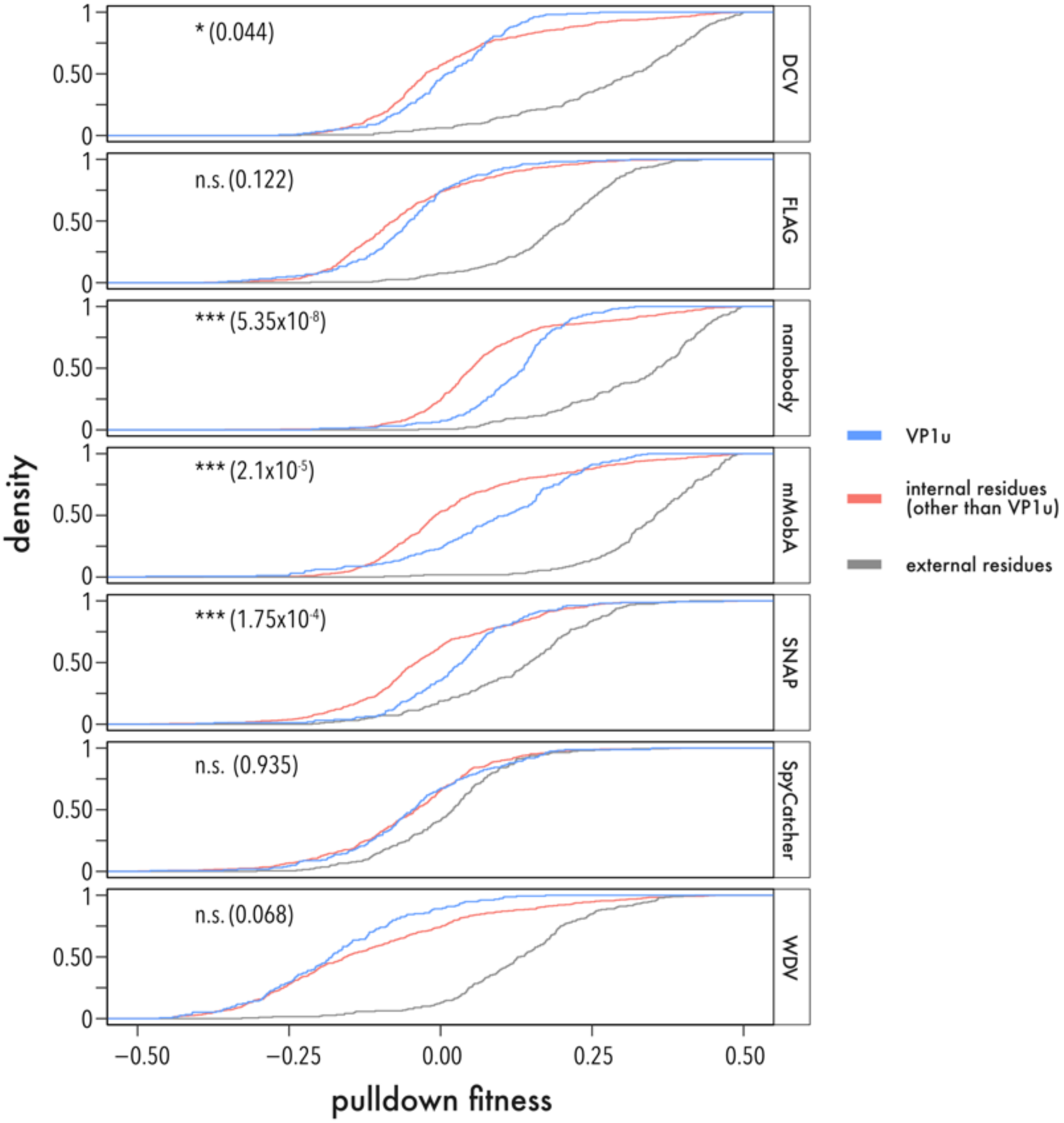

Figure S9

Distribution of pulldown fitness by residue location. Cumulative density function of pulldown fitness for each inserted motif stratified by residue location; within VP1u (blue), buried or exposed inside the capsid and not in VP1u (red), external residues (gray). Significance of distribution differences was tested using a two-sided, two-sample Kolmogorov-Smirnov test. Significance level and p values are shown.

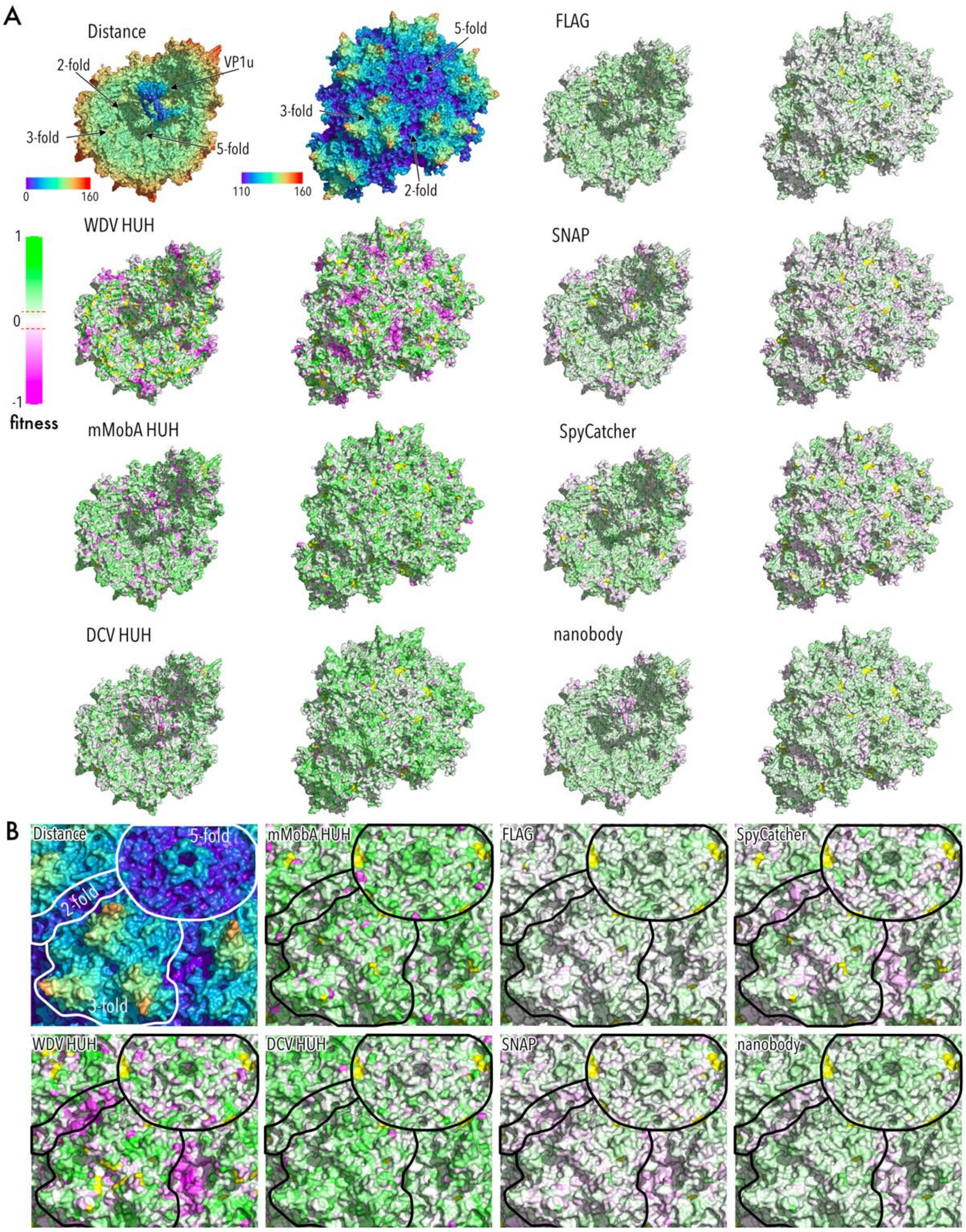

Figure S10

Binding fitness of AAV domain insertion libraries mapped to the capsid structure. (A) Top left corner: AAV-DJ capsid structure view from the inside (left) and outside (right) radially color-cued. 2-, 3-, and 5-fold axes are indicated. VP1u domain was modeled using RoseTTAFold (98) and manually positioned. All other structures show binding fitness heatmaps of the indicated domain insertions. Green indicates higher and magenta lower fitness than AAV-DJ (white) (RCSB PDB 7KFR). (B) Zoom of the outside structures from (A). 2-, 3-, and 5-fold axes are outlined.

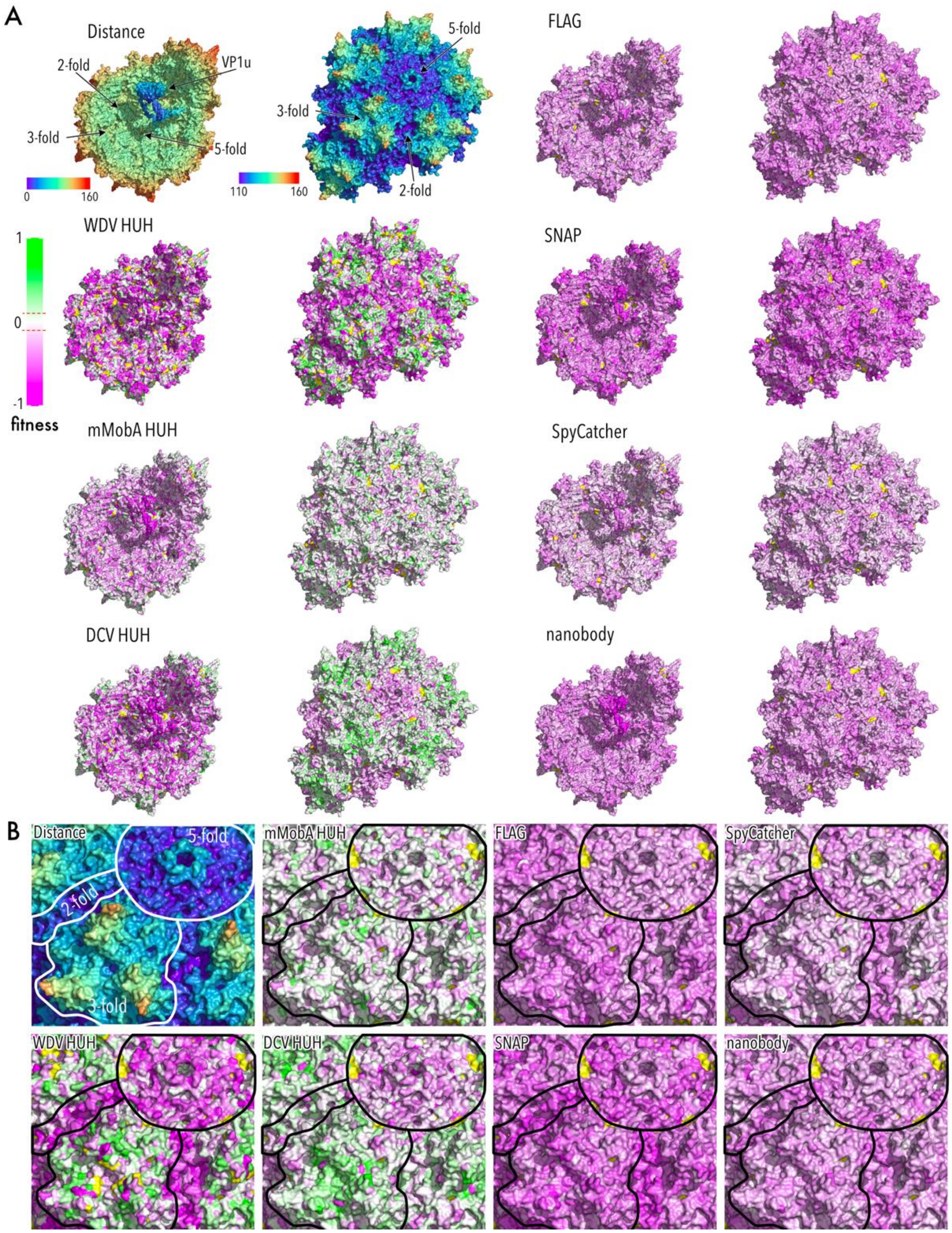

Figure S11

Uptake fitness of AAV domain insertion libraries mapped to the capsid structure. (A) Top left corner: AAV-DJ capsid structure view from the inside (left) and outside (right) radially color-cued. 2-, 3-, and 5-fold axes are indicated. VP1u domain was modeled using RoseTTAFold (98) and manually positioned. All other structures show uptake fitness heatmaps of the indicated domain insertions. Green indicates higher and magenta lower fitness than AAV-DJ (white) (RCSB PDB 7KFR). (B) Zoom of the outside structures from (A). 2-, 3-, and 5-fold axes are outlined.

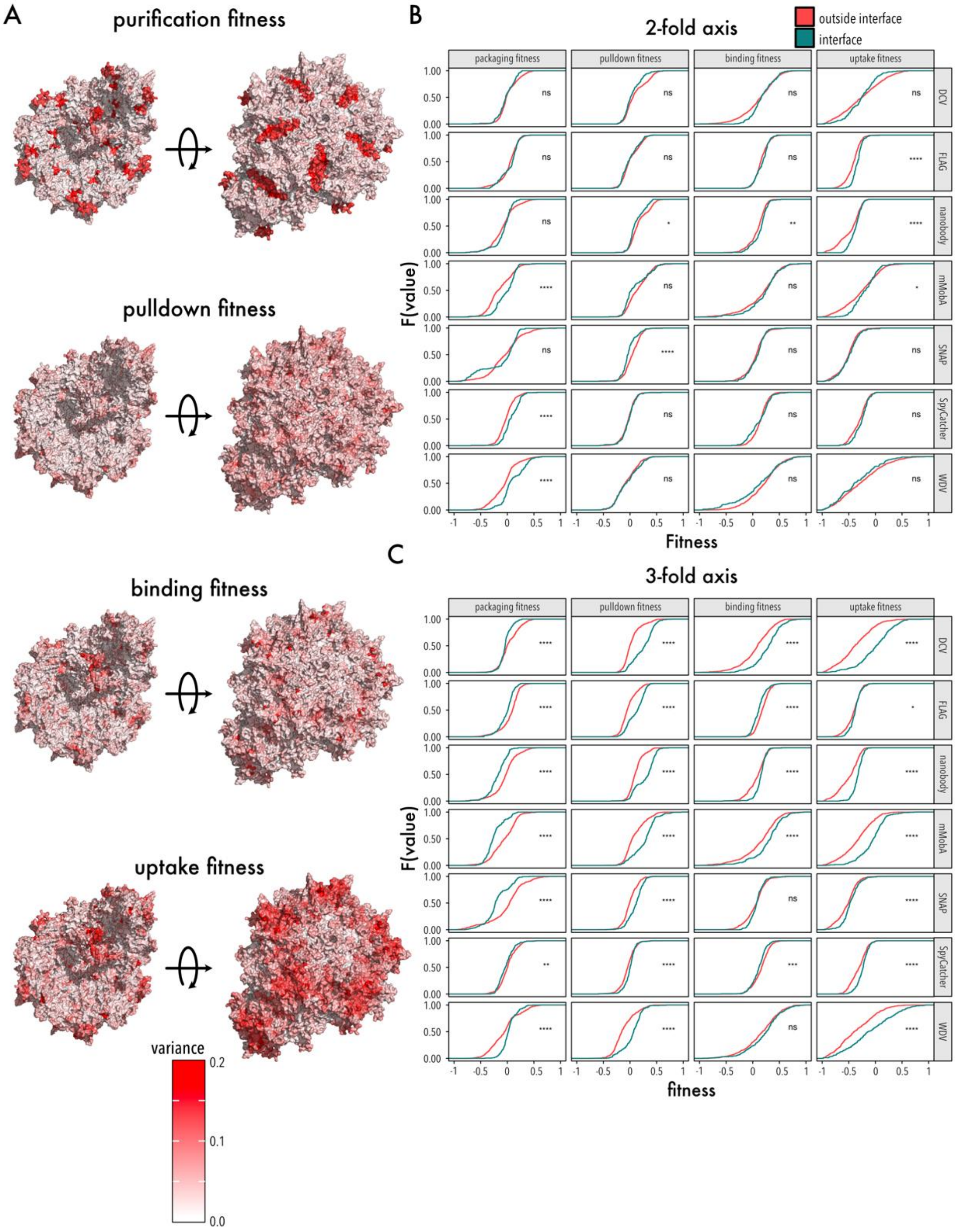

Figure S12

Variance of all measured fitness assays. (A) Variance of different fitness measures from all domain insertion libraries mapped to the AAV capsid structure. The capsid inside (left) and the capsid outside (right) are shown (RCSB PDB 7KFR). (B) Empirical cumulative density insertional fitness of residues within (petrol green) and outside (red) at the 2-fold axis (top) and 3-fold axis (bottom). Significance of distribution differences was tested using a two-sided, two-sample Kolmogorov-Smirnov test. Significance levels are shown (**** < 0.0001, *** < 0.001, ** < 0.01, * < 0.05).

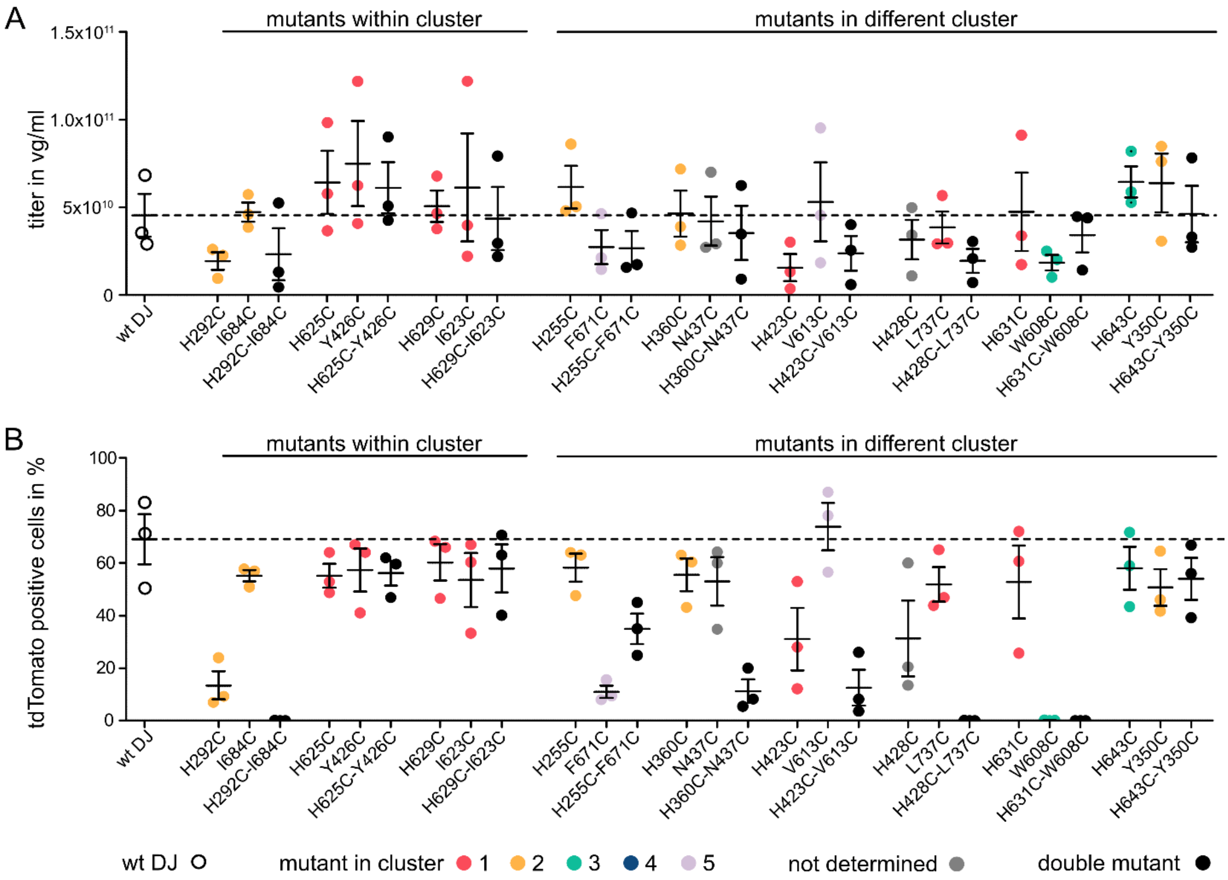

Figure S13

Packaging and infection fitness of cysteine mutants. (A) Crude lysate packaging titers quantified via qPCR. (B) Infection fitness quantified by measuring the percentage of tdTomato positive cells 48 hours post transduction with an MOI of 1×10^4 vg/cell. Data are means ± SEM. Data points of single mutants are colored by cluster membership, missing residues are gray, double mutants are black, and wildtype AAV-DJ fitness is shown as open circles and horizontal dashed line.

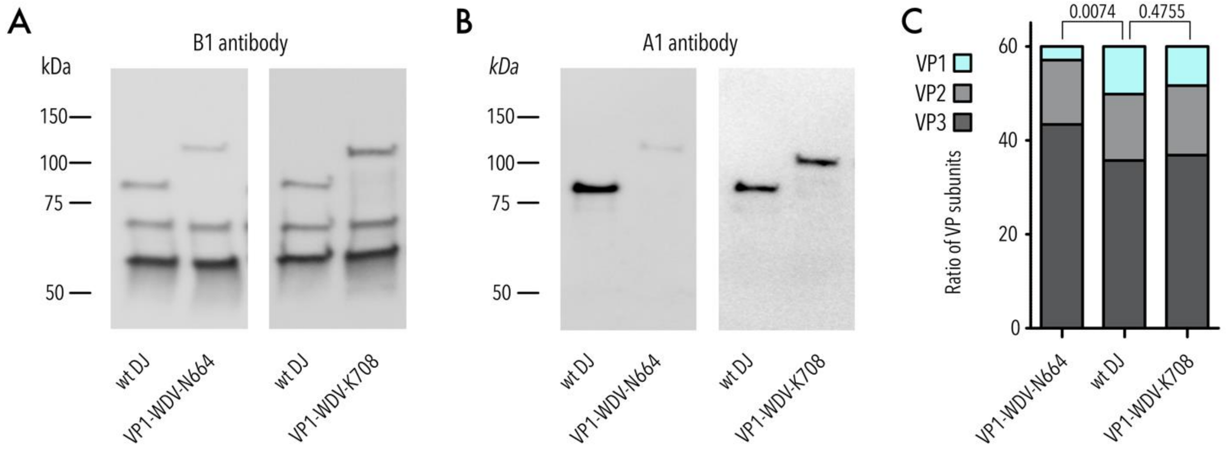

Figure S14

Quantification of VP ratios of WDV insertion variants N664 and K708. (A) Representative Western blot image of AAV domain insertion libraries stained with B1 antibody (detecting VP1, VP2 and VP3 subunits). (B) Representative Western blot image of AAV domain insertion libraries stained with A1 antibody (detecting VP1 subunits). (C) Western blot quantification of VP1, VP2, and VP3 subunits. Data are means (n=3). VP1 content varies significantly (one-way ANOVA p-value: 0.00993, Dunnett's test for pairwise comparison with wildtype AAV-DJ as control: N664 p-value 0.0074; K708 p-value 0.4755.

Table S1

Plasmids and libraries used in this study.

Plasmids not generated, but used for this study			
#	Name	Encodes/ Use	Origin
01	Adeno-helper	Adenohelper proteins for AAV productions	Cellbiolabs
02	AAV-DJ	rep2-capDJ for packaging of AAV-DJ	Cellbiolabs
03	tdTomato	ITR_CAG-tdTomato-WPRE	based on Addgene Plasmid #105554
04	DJ-M1K	rep2-capDJ mutated VP1 start codon	Schmidt Lab (Alina Zdechlik)
05	DJ-VP1	DJ VP1 only (mutated start sites for VP2 & VP3), HA tag instead of HBD; used as cloning intermediate	Schmidt Lab (Alina Zdechlik)
06	CMV-GFP-GPI	Expression of GFP at outer cell membrane	Schmidt Lab (Alina Zdechlik)
07	pUC19	Stuffer plasmid	ThermoFisher
Plasmids and libraries generated for this study			
#	Name	Use	Origin
08	library_entry	ITR_EFS-driven miRFP670nano & p40 with BsmBI sites to insert DJ-VP1 chlor; used control plasmid	Schmidt Lab (Mareike Hoffmann)
09	DJ-VP1_SilMut	ITR_EFS-driven miRFP670nano & p40-driven DJ-VP1 with silent mutations	Schmidt Lab (Mareike Hoffmann)
10	DJ-H255C	rep2-capDJ-H255C; cysteine mutant	Schmidt Lab (Mareike Hoffmann)
11	DJ-F671C	rep2-capDJ-F671C; cysteine mutant	Schmidt Lab (Mareike Hoffmann)
12	DJ-H255C-F671C	rep2-capDJ-H255C-F671C; cysteine mutant	Schmidt Lab (Mareike Hoffmann)
13	DJ-H292C	rep2-capDJ-H292C; cysteine mutant	Schmidt Lab (Mareike Hoffmann)
14	DJ-I684C	rep2-capDJ-I684C; cysteine mutant	Schmidt Lab (Mareike Hoffmann)
15	DJ-H292C-I684C	rep2-capDJ-H292C-I684C; cysteine mutant	Schmidt Lab (Mareike Hoffmann)
16	DJ-H360C	rep2-capDJ-H360C; cysteine mutant	Schmidt Lab (Mareike Hoffmann)
17	DJ-N437C	rep2-capDJ-N437C; cysteine mutant	Schmidt Lab (Mareike Hoffmann)
18	DJ-H360C-N437C	rep2-capDJ-H360C-N437C; cysteine mutant	Schmidt Lab (Mareike Hoffmann)
19	DJ-H423C	rep2-capDJ-H423C; cysteine mutant	Schmidt Lab (Mareike Hoffmann)
20	DJ-V613C	rep2-capDJ-V613C; cysteine mutant	Schmidt Lab (Mareike Hoffmann)
21	DJ-H423C-V613C	rep2-capDJ-H423C-V613C; cysteine mutant	Schmidt Lab (Mareike Hoffmann)
22	DJ-H428C	rep2-capDJ-H428C; cysteine mutant	Schmidt Lab (Mareike Hoffmann)
23	DJ -L737C	rep2-capDJ -L737C; cysteine mutant	Schmidt Lab (Mareike Hoffmann)
24	DJ-H428C-L737C	rep2-capDJ-H428C-L737C; cysteine mutant	Schmidt Lab (Mareike Hoffmann)
25	DJ-H625C	rep2-capDJ-H625C; cysteine mutant	Schmidt Lab (Mareike Hoffmann)
26	DJ-Y426C	rep2-capDJ-Y426C; cysteine mutant	Schmidt Lab (Mareike Hoffmann)
27	DJ-H625C-Y426C	rep2-capDJ-H625C-Y426C; cysteine mutant	Schmidt Lab (Mareike Hoffmann)

28	DJ-H629C	rep2-capDJ-H629C; cysteine mutant	Schmidt Lab (Mareike Hoffmann)
29	DJ-I623C	rep2-capDJ-I623C; cysteine mutant	Schmidt Lab (Mareike Hoffmann)
30	DJ-H629C-I623C	rep2-capDJ-H629C-I623C; cysteine mutant	Schmidt Lab (Mareike Hoffmann)
31	DJ-H631C	rep2-capDJ-H631C; cysteine mutant	Schmidt Lab (Mareike Hoffmann)
32	DJ-W608C	rep2-capDJ-W608C; cysteine mutant	Schmidt Lab (Mareike Hoffmann)
33	DJ-H631C-W608C	rep2-capDJ-H631C-W608C; cysteine mutant	Schmidt Lab (Mareike Hoffmann)
34	DJ-H643C	rep2-capDJ-H643C; cysteine mutant	Schmidt Lab (Mareike Hoffmann)
35	DJ-Y350C	rep2-capDJ-Y350C; cysteine mutant	Schmidt Lab (Mareike Hoffmann)
36	DJ-H643C-Y350C	rep2-capDJ-H643C-Y350C; cysteine mutant	Schmidt Lab (Mareike Hoffmann)
37	DJ-VP1-L256-WDV	p40-driven DJ-VP1 with WDV insertion L256	Schmidt Lab (Mareike Hoffmann)
38	DJ-VP1-S268-WDV	p40-driven DJ-VP1 with WDV insertion S268	Schmidt Lab (Mareike Hoffmann)
39	DJ-VP1-K311-WDV	p40-driven DJ-VP1 with WDV insertion K311	Schmidt Lab (Mareike Hoffmann)
40	DJ-VP1T331-WDV	p40-driven DJ-VP1 with WDV insertion T331	Schmidt Lab (Mareike Hoffmann)
41	DJ-VP1-E349-WDV	p40-driven DJ-VP1 with WDV insertion E349	Schmidt Lab (Mareike Hoffmann)
42	DJ-VP1-T414-WDV	p40-driven DJ-VP1 with WDV insertion T414	Schmidt Lab (Mareike Hoffmann)
43	DJ-VP1-S244-WDV	p40-driven DJ-VP1 with WDV insertion S244	Schmidt Lab (Mareike Hoffmann)
44	DJ-VP1-N664-WDV	p40-driven DJ-VP1 with WDV insertion N664	Schmidt Lab (Mareike Hoffmann)
45	DJ-VP1-Y702-WDV	p40-driven DJ-VP1 with WDV insertion Y702	Schmidt Lab (Mareike Hoffmann)
46	DJ-VP1-K708-WDV	p40-driven DJ-VP1 with WDV insertion K708	Schmidt Lab (Mareike Hoffmann)
lib01	DJ-VP1 chlor	Template for domain insertion library, contains handle with chloramphenicol	Schmidt Lab (Mareike Hoffmann)
lib02	pAAV_DJ-VP1-chlor	ITR_EFS-driven miRFP670nano & p40-driven DJ-VP1 with chlor handle	Schmidt Lab (Mareike Hoffmann)
lib03	pAAV_DJ-VP1-nanobody	ITR_EFS-driven miRFP670nano & p40-driven DJ-VP1 with nanobody insertion	Schmidt Lab (Mareike Hoffmann)
lib04	pAAV_DJ-VP1-SNAP	ITR_EFS-driven miRFP670nano & p40-driven DJ-VP1 with SNAP insertion	Schmidt Lab (Mareike Hoffmann)
lib05	pAAV_DJ-VP1-SpyCatcher	ITR_EFS-driven miRFP670nano & p40-driven DJ-VP1 with SpyCatcher insertion	Schmidt Lab (Mareike Hoffmann)
lib06	pAAV_DJ-VP1-mMobA	ITR_EFS-driven miRFP670nano & p40-driven DJ-VP1 with mMobA insertion	Schmidt Lab (Mareike Hoffmann)
lib07	pAAV_DJ-VP1-WDV	ITR_EFS-driven miRFP670nano & p40-driven DJ-VP1 with WDV insertion	Schmidt Lab (Mareike Hoffmann)
lib08	pAAV_DJ-VP1-FLAG	ITR_EFS-driven miRFP670nano & p40-driven DJ-VP1 with FLAG insertion	Schmidt Lab (Mareike Hoffmann)
lib09	pAAV_DJ-VP1-DCV	ITR_EFS-driven miRFP670nano & p40-driven DJ-VP1 with DCV insertion	Schmidt Lab (Mareike Hoffmann)

Table S2

Sequencing statistics.

Sequencing Run	Pool Name	Assay	Repl.	Total Reads	Mean Quality R1	Mean Quality R2	Motif	Aligned Reads	Pos	Median Reads / Position	Coverage [x-fold]
Schmidt_Project_053	S1	Insertion Library	1	49,263,317	34.8	33.8	DCV	984,082	744	1295	1,323
							FLAG	440,403		564	592
							GFPnb	612,028		768	823
							mMobA	860,533		1187	1,157
							SNAP	374,315		450	503
							SpyCatcher	387,705		503	521
							WDV	663,006		849	891
	S2	Packaging Assay	1	51,060,989	34.8	33.9	DCV	866,748	744	996	1,165
							FLAG	588,126		757	790
							GFPnb	596,785		745	802
							mMobA	972,338		1280	1,307
							SNAP	355,788		448	478
							SpyCatcher	464,490		566	624
							WDV	495,047		562	665
	S3	Pulldown Assay	1	47,622,985	34.8	33.4	DCV	1,103,510	744	1058	1,483
							FLAG	479,651		557	645
							GFPnb	773,476		934	1,040
							mMobA	953,608		1099	1,282
							SNAP	431,198		515	580
							SpyCatcher	1,664		2	2
							WDV	684,376		731	920
	S4	Binding Assay	1	37,616,155	34.8	33.8	DCV	1,753	744	1	2
							FLAG	544,918		598	732
							GFPnb	562,553		611	756
							mMobA	495,428		611	666
							SNAP	311,261		355	418
							SpyCatcher	412,666		474	555
							WDV	359,617		128	483
	S5	Uptake Assay	1	47,345,415	34.7	33.4	DCV	1,781	744	2	2
							FLAG	308,480		360	415
							GFPnb	235,074		257	316
							mMobA	1,330,134		584	1,788
							SNAP	289,337		300	389
							SpyCatcher	728,389		832	979

							WDV	490,064		516	659
	S6	Infectivity Assay	1	43,873,293	34.8	33.6	DCV	1,597	744	2	2
							FLAG	530,282		680	713
							GFPnb	685,511		762	921
							mMobA	556,769		527	748
							SNAP	248,758		169	334
							SpyCatcher	383,865		424	516
							WDV	434,667		393	584
Schmidt_Project_054	S1	Insertion Library	1	51,407,231	35.1	34.7	DCV	763,808	744	997	1,027
							FLAG	540,227		694	726
							GFPnb	800,432		1018	1,076
							mMobA	798,364		1115	1,073
							SNAP	386,969		490	520
							SpyCatcher	429,433		555	577
							WDV	441,373		567	593
	S2	Packaging Assay	1	52,569,434	35.1	35.2	DCV	792,792	744	1004	1,066
							FLAG	579,228		754	779
							GFPnb	753,802		945	1,013
							mMobA	731,258		982	983
							SNAP	360,936		456	485
							SpyCatcher	439,536		580	591
							WDV	446,429		513	600
	S3	Pulldown Assay	1	55,102,309	35.2	34.8	DCV	867,430	744	1033	1,166
							FLAG	584,332		704	785
							GFPnb	878,514		1068	1,181
							mMobA	831,938		1134	1,118
							SNAP	364,218		452	490
							SpyCatcher	414,933		539	558
							WDV	421,941		450	567
	S4	Binding Assay	1	49,251,857	35.2	35	DCV	634,851	744	769	853
							FLAG	451,741		602	607
							GFPnb	561,059		700	754
							mMobA	617,489		789	830
							SNAP	256,278		315	344
							SpyCatcher	334,592		448	450
							WDV	367,036		400	493
	S5	Uptake Assay	1	54,099,860	35.2	35	DCV	815,491	744	904	1,096
							FLAG	510,011		670	685
							GFPnb	630,885		774	848

							mMobA	780,744		1049	1,049
							SNAP	284,480		336	382
							SpyCatcher	431,248		563	580
							WDV	459,667		408	618
	S6	Infectivity Assay	1	47,910,960	35.1	34.6	DCV	534,941	744	658	719
							FLAG	414,577		555	557
							GFPnb	421,517		507	567
							mMobA	466,958		622	628
							SNAP	179,921		215	242
							SpyCatcher	249,392		332	335
							WDV	318,616		350	428

Table S3

DNA oligos used in this study.

Use/ Target	**Direction**	**Sequence**	**Modification**
qPCR/ p40[20]	forward	TTTCCGGTGGGCAAAGG	
	reverse	GCTCACTTATATCTGCGTCACT	
qPCR/ CMV-enhancer[21]	forward	AACGCCAATAGGGACTTTCC	
	reverse	GGGCGTACTTGGCATATGAT	
NGS amplification PCR / cap	forward	CTGGTCAATGTGGATTTGGATGACTGC	
	reverse	GCAGACCAAAGTTCAACTGAAACGAATCAAC	
Pulldown/mMobA[22]	-	CCAGTTTCTCGAAGAGAAACCGGTAAGTGCACCCTCCC	3' Biotin
Pulldown/WDV[23]	-	TAATATTACCGGATGCCGCGC	3' Biotin
Pulldown/DCV[23]	-	TATTATTACCAGAAATGATGA	3' Biotin
Binding, Internalization, and Infectivity/WDV[23]	-	TAATATTACCGGATGCCGCGC	3' Amino Modifier C6 dT

Supplemental References

1. Girod, A., Wobus, C. E., Zádori, Z., Ried, M., Leike, K., Tijssen, P., Kleinschmidt, J. A., and Hallek, M. (2002). The VP1 capsid protein of adeno-associated virus type 2 is carrying a phospholipase A2 domain required for virus infectivity. J Gen Virol *83*, 973-978.
2. Zádori, Z., Szelei, J., Lacoste, M. C., Li, Y., Gariépy, S., Raymond, P., Allaire, M., Nabi, I. R., and Tijssen, P. (2001). A viral phospholipase A2 is required for parvovirus infectivity. Dev Cell *1*, 291-302.
3. Venkatakrishnan, B., Yarbrough, J., Domsic, J., Bennett, A., Bothner, B., Kozyreva, O. G., Samulski, R. J., Muzyczka, N., McKenna, R., and Agbandje-McKenna, M. (2013). Structure and dynamics of adeno-associated virus serotype 1 VP1-unique N-terminal domain and its role in capsid trafficking. J Virol *87*, 4974-4984.
4. Grieger, J. C., Snowdy, S., and Samulski, R. J. (2006). Separate basic region motifs within the adeno-associated virus capsid proteins are essential for infectivity and assembly. J Virol *80*, 5199-5210.
5. Mateu, M. G. (2013). Assembly, stability and dynamics of virus capsids. Arch Biochem Biophys *531*, 65-79.
6. Medrano, M., Fuertes, M. Á., Valbuena, A., Carrillo, P. J., Rodríguez-Huete, A., and Mateu, M. G. (2016). Imaging and Quantitation of a Succession of Transient Intermediates Reveal the Reversible Self-Assembly Pathway of a Simple Icosahedral Virus Capsid. J Am Chem Soc *138*, 15385-15396.
7. Large, E. E., and Chapman, M. S. (2023). Adeno-associated virus receptor complexes and implications for adeno-associated virus immune neutralization. Front Microbiol *14*, 1116896.
8. Lerch, T. F., O'Donnell, J. K., Meyer, N. L., Xie, Q., Taylor, K. A., Stagg, S. M., and Chapman, M. S. (2012). Structure of AAV-DJ, a retargeted gene therapy vector: cryo-electron microscopy at 4.5 Å resolution. Structure *20*, 1310-1320.
9. Meyer, N. L., Hu, G., Davulcu, O., Xie, Q., Noble, A. J., Yoshioka, C., Gingerich, D. S., Trzynka, A., David, L., Stagg, S. M. et al. (2019). Structure of the gene therapy vector, adeno-associated virus with its cell receptor, AAVR. Elife *8*, e44707.
10. Pillay, S., Meyer, N. L., Puschnik, A. S., Davulcu, O., Diep, J., Ishikawa, Y., Jae, L. T., Wosen, J. E., Nagamine, C. M., Chapman, M. S. et al. (2016). An essential receptor for adeno-associated virus infection. Nature *530*, 108-112.
11. Stagg, S. M., Yoshioka, C., Davulcu, O., and Chapman, M. S. (2022). Cryo-electron Microscopy of Adeno-associated Virus. Chem Rev *122*, 14018-14054.
12. Xie, Q., Bu, W., Bhatia, S., Hare, J., Somasundaram, T., Azzi, A., and Chapman, M. S. (2002). The atomic structure of adeno-associated virus (AAV-2), a vector for human gene therapy. Proc Natl Acad Sci U S A *99*, 10405-10410.
13. Meyer, N. L., and Chapman, M. S. (2022). Adeno-associated virus (AAV) cell entry: structural insights. Trends Microbiol *30*, 432-451.
14. Horowitz, E. D., Finn, M. G., and Asokan, A. (2012). Tyrosine cross-linking reveals interfacial dynamics in adeno-associated viral capsids during infection. ACS Chem Biol *7*, 1059-1066.
15. Gerlach, B., Kleinschmidt, J. A., and Böttcher, B. (2011). Conformational changes in adeno-associated virus type 1 induced by genome packaging. J Mol Biol *409*, 427-438.

16. Levy, H. C., Bowman, V. D., Govindasamy, L., McKenna, R., Nash, K., Warrington, K., Chen, W., Muzyczka, N., Yan, X., Baker, T. S. et al. (2009). Heparin binding induces conformational changes in Adeno-associated virus serotype 2. J Struct Biol *165*, 146-156.
17. DiPrimio, N., Asokan, A., Govindasamy, L., Agbandje-McKenna, M., and Samulski, R. J. (2008). Surface loop dynamics in adeno-associated virus capsid assembly. J Virol *82,* 5178-5189.
18. Bleker, S., Pawlita, M., and Kleinschmidt, J. A. (2006). Impact of capsid conformation and Rep-capsid interactions on adeno-associated virus type 2 genome packaging. J Virol *80*, 810-820.
19. Drouin, L. M., Lins, B., Janssen, M., Bennett, A., Chipman, P., McKenna, R., Chen, W., Muzyczka, N., Cardone, G., Baker, T. S. et al. (2016). Cryo-electron Microscopy Reconstruction and Stability Studies of the Wild Type and the R432A Variant of Adeno-associated Virus Type 2 Reveal that Capsid Structural Stability Is a Major Factor in Genome Packaging. J Virol *90*, 8542-8551.
20. Nonnenmacher, M., Wang, W., Child, M. A., Ren, X. Q., Huang, C., Ren, A. Z., Tocci, J., Chen, Q., Bittner, K., Tyson, K. et al. (2021). Rapid evolution of blood-brain-barrier-penetrating AAV capsids by RNA-driven biopanning. Mol Ther Methods Clin Dev *20*, 366-378.
21. Negrete, A., and Kotin, R. M. (2007). Production of recombinant adeno-associated vectors using two bioreactor configurations at different scales. J Virol Methods *145*, 155-161.
22. Lovendahl, K. N., Hayward, A. N., and Gordon, W. R. (2017). Sequence-Directed Covalent Protein-DNA Linkages in a Single Step Using HUH-Tags. J Am Chem Soc *139*, 7030-7035.
23. Tompkins, K. J., Houtti, M., Litzau, L. A., Aird, E. J., Everett, B. A., Nelson, A. T., Pornschloegl, L., Limón-Swanson, L. K., Evans, R. L., Evans, K. et al. (2021). Molecular underpinnings of ssDNA specificity by Rep HUH-endonucleases and implications for HUH-tag multiplexing and engineering. Nucleic Acids Res *49*, 1046-1064.